nanomaterials

MDPI

Communication

Single-Step Direct Hydrothermal Growth of $NiMoO_4$ Nanostructured Thin Film on Stainless Steel for Supercapacitor Electrodes

V. Kannan [1], Hyun-Jung Kim [2], Hyun-Chang Park [2] and Hyun-Seok Kim [2,*]

[1] Millimeter-Wave Innovation Technology Research Center (MINT), Dongguk University-Seoul, Seoul 04620, Korea; kannan@dongguk.edu

[2] Division of Electronics and Electrical Engineering, Dongguk University-Seoul, Seoul 04620, Korea; best7hj@daum.net (H.-J.K.); hcpark@dongguk.edu (H.-C.P.)

* Correspondence: hyunseokk@dongguk.edu; Tel.: +82-2-2260-3996; Fax: +82-2-2277-8735

Received: 24 June 2018; Accepted: 21 July 2018; Published: 24 July 2018

Abstract: We report a facile and direct growth of $NiMoO_4$ nanostructures on a nonreactive stainless steel substrate using a single-step hydrothermal method and investigated hydrothermal growth duration effects on morphology and electrochemical characteristics. The highest specific capacitances of 341, 619, and 281 F/g were observed for $NiMoO_4$ with 9, 18, and 27 h growth, respectively, at 1 A/g. Thus, grown samples preserved almost 59% of maximum specific capacitance at a high current density of 10 A/g. All samples exhibited a respectable cycling stability over 3000 charge-discharge operations. $NiMoO_4$ grown for 18 h exhibited 7200 W/kg peak power density at 14 Wh/kg energy density. Thus, the proposed single-step hydrothermal growth is a promising route to obtain $NiMoO_4$ nanostructures and other metal oxide electrodes for supercapacitor applications.

Keywords: $NiMoO_4$; nanostructures; hydrothermal; supercapacitor; stainless steel

1. Introduction

Supercapacitors have been widely studied as candidates for energy storage systems due to their large power density, rapid charge-discharge, excellent rate capabilities, and good endurance [1–3]. They have been used in tandem with rechargeable storage devices and fuel cells, and they have been broadly applied for electric vehicles, electrical grid buffers, space applications, and memory system power back-up. In the recent past, there has been significant surge of research in transition metal oxides-based supercapacitors due to their multiple oxidation states and reversible redox reaction capabilities [4–6]. However, progress in supercapacitor electrode materials has been constrained by high cost (e.g., RuO_2) or environmental impact (e.g., metal sulfides) [7–9].

Metal oxides with two transition metals have also been studied to take advantage of their variable oxidation states, excellent electrical conduction, and enhanced pseudo-capacitance characteristics, such as $CoMoO_4$ [10,11], $NiCo_2O_4$ [6], $ZnWO_4$ [12], and $NiMoO_4$ [13]. $NiMoO_4$ is a promising binary metal oxide due to its potential for high specific capacitance arising from the excellent electrochemical nature of the Ni ion, although practical electrode use is deterred by its poor electrical conductivity. Intricate characteristics of the molybdate also complicate $NiMoO_4$ nanostructure growth [14,15]. Hence, it is important to identify easier preparation routes for $NiMoO_4$ nanostructure thin films with distinct morphologies and superior supercapacitor characteristics.

There is a promising route to grow the nanostructures directly on conducting substrates [16], countering inherent low metal oxide electrical conductivity and, hence, considerably enhancing electrochemical performance. There are many reports of $NiMoO_4$ supercapacitor performance on Ni

foam substrates [14–18]. However, the $NiMoO_4$ on Ni foam (usually coated with a binder as a slurry) is often dominated by the Ni foam contribution to overall electrochemical performance, making it difficult to identify the exact supercapacitance value of the desired electrode material. Only $NiMoO_4$ nanostructure synthesis on nonreactive substrates has been reported previously, such as stainless steel (SS) and carbon [16,19], without exploring its electrochemical characteristics. However, there are no reports available detailing the electrochemical performance of $NiMoO_4$ thin film nanostructures on nonreactive substrate such as stainless steel. Here we intend to exclusively evaluate the electrochemical performance of $NiMoO_4$ thin film nanostructures, without the hindrance of substrate contribution.

This study reports on the binder-free growth of $NiMoO_4$ nanostructures on SS substrate using a facile, single-step hydrothermal technique. The optimal growth time was identified by studying $NiMoO_4$ thin films grown for 9, 18, and 27 h, keeping other deposition conditions constant. Nanostructured $NiMoO_4$ grown on SS substrate exhibited high specific capacitance, good cycling stability, and enhanced rate capability. The proposed technique offers a promising, environmentally friendly, and relatively low cost direct route to obtain high supercapacitance $NiMoO_4$ nanostructures.

2. Materials and Methods

2.1. $NiMoO_4$ Nanostructure Growth Process

Molybdenum chloride (1.5 mmol) was mixed with methanol (50 mL) and stirred for 10 min. Nickel chloride solution (1.5 mmol) was added and stirred for a further 10 min, then EDTA (1.5 mmol) was added and stirred for 1 h. After forming a clear solution, 1 mL H_2O_2 and 1 mL HNO_3 were added and stirred for 10 min. The solution was transferred to a Teflon container that already contained a pre-cleaned SS substrate with 1 cm $\times$ 2 cm exposed area. The complete setup was placed in a stainless steel autoclave at 180 °C. In order to identify optimal growth time, experiments were conducted with wide ranging growth durations from 9 to 36 h. Three samples were identified with 9, 18, and 27 h growth duration and labeled as NMO-9, NMO-18, and NMO-27, respectively, due to their superior electrochemical performance over the other samples. The grown films are then harvested, washed with deionized water, and dried with N_2 gas.

2.2. Materials Characterization

The obtained thin films were characterized using a field emission scanning electron microscope (FE-SEM, Hitachi-S-4800, Huntington Beach, CA, USA), transmission electron microscope (TEM, JEM-2100F, JEOL, Akishima, Tokyo, Japan), and high angle annular dark field imaging (HAADF) scanning transmission electron microscope (STEM, JEM-2100F, JEOL, Akishima, Tokyo, Japan). Electrochemical measurements were performed in a 2 M KOH aqueous solution using a standard three-electrode electrochemical cell in Versa-stat-3. $NiMoO_4$ served as the working electrode, with a saturated calomel electrode (SCE) and graphite rod as reference and counter electrodes, respectively.

3. Results

FE-SEM morphology of the grown films for the durations of 9 h, 18 h, and 27 h are shown in Figure 1. $NiMoO_4$ nanostructures are evident for all the films grown for different durations, exhibiting a stacked structure with $NiMoO_4$ nanograins. TEM analyses were carried out only on sample NMO-18 due to its superior electrochemical performance in comparison with NMO-9 and NMO-27. Figure 2a,b show typical TEM images for the 18 h sample, revealing crystalline $NiMoO_4$ grain-like structure. From the observed twist dislocations in Figure 2b, it can be inferred that the crystals are composed of narrow platelets. Figure 2c shows a typical high resolution transmission electron microscope (HRTEM) image from a single nanograin. The interplanar distance (0.39 nm) corresponds to monoclinic $NiMoO_4$ $(02\bar{1})$ crystal planes (JCPDS: 45-0142). Figure 2d shows the selected area diffraction (SAED) pattern, which confirms the polycrystalline nature. Figure 2e–h shows the HAADF-STEM electron, O, Ni,

and Mo mappings, respectively, using the same scale is the TEM images. Ni, Mo, and O are relatively uniformly distributed, which is confirmed by the elemental line mapping, as shown in Figure 2i.

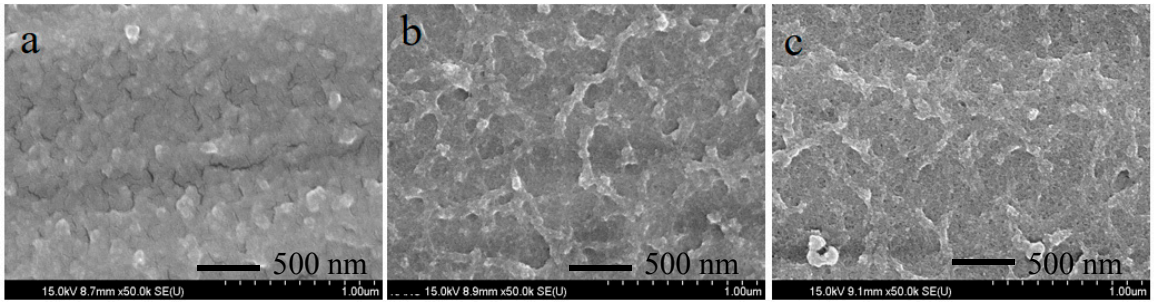

Figure 1. Typical field emission scanning electron microscope (FE-SEM) images for (**a**) NMO-9; (**b**) NMO-18; and (**c**) NMO-27 samples.

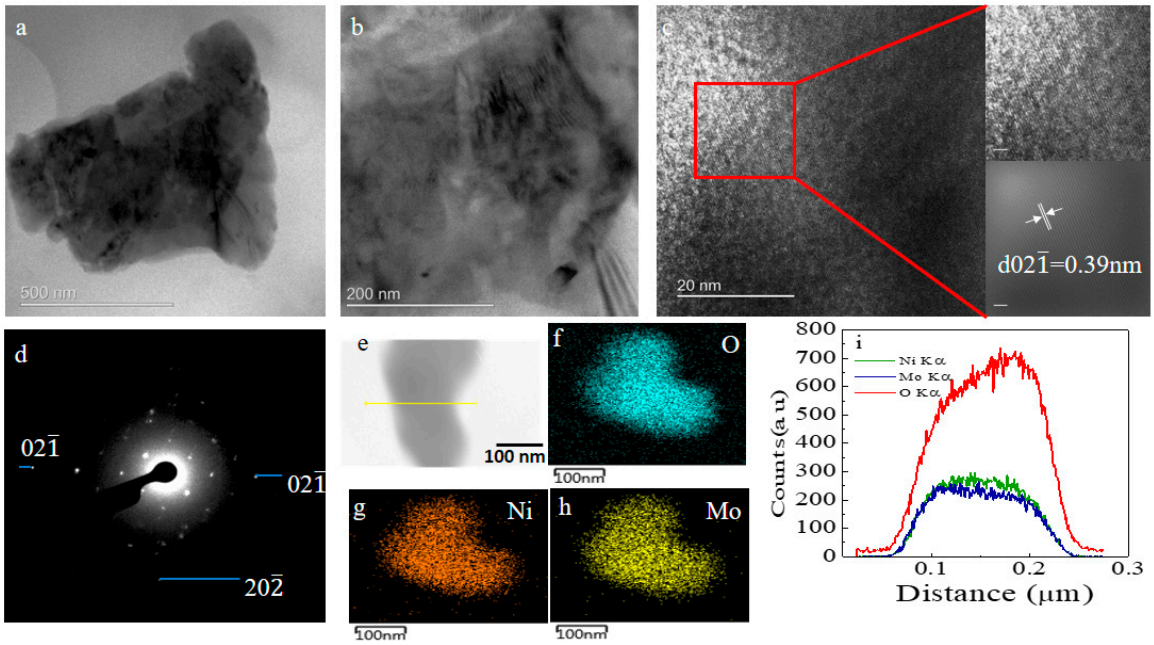

Figure 2. The transmission electron microscope (TEM) image for a single $NiMoO_4$ nanograin grown for 18 h at (**a**) low and (**b**) high magnification; (**c**) The high resolution transmission electron microscope (HRTEM) image with d spacing noted; (**d**) The selected area diffraction (SAED) pattern of the same sample showing respective planes. High angle annular dark field imaging scanning transmission electron microscope (HAADF-STEM) elemental mapping for a selected area showing (**e**) the electron with line mapping; (**f**) oxygen; (**g**) nickel; (**h**) molybdenum; and (**i**) line mapping, showing the counts of Mo, Ni, and O.

The electrochemical characteristics of the electrode are mainly dependent on their dimensions and morphologies [20,21]. Electrochemical measurements of $NiMoO_4$ nanostructure were performed in 2 M KOH electrolyte. Figure 3a shows the cyclic voltammograms (CV) for hydrothermally grown $NiMoO_4$ at different durations (100 mV/s scan rate), over the potential range of 0–0.43 V (versus SCE). Each CV plot exhibits distinct redox peaks, indicating that the observed capacitance properties can be described by Faradic reactions [22,23]. The NMO-18 sample had the largest area under the CV curve compared with NMO-9 and NMO-27.

Figure 3b–d show NMO-9, NMO-18, and NMO-27 CVs, respectively, for various scan rates. The CV curve shapes are almost unchanged for the different scan rates, indicating near ideal capacitive

characteristics. Voltage corresponding to the oxidation peak moved in the positive direction as the scan rate increased, whereas the reduction peak moved in the negative direction, which can be attributed to electrode's internal resistance [24].

The surface area accessible for electrochemical reactions can be estimated from the electrochemically active surface area (ECSA). Initially, the non-Faradic capacitive current was obtained from the linear region of the CV curves,

$$i_{DL} = C_{DL} \times \nu \quad (1)$$

where i_{DL} is the capacitive current, C_{DL} is the specific capacitance in the non-Faradic region, and ν is the scan rate. Electrochemical capacitance was estimated for each sample at the various scan rates, and ECSA was calculated from

$$\text{ECSA} = C_{DL}/C_s \quad (2)$$

where C_s is the specific capacitance of the standard electrode in an alkaline electrolyte [25]. We chose the non-Faradic region as 0.21–0.23 V, as shown in Figure 4a. Figure 4b shows the i_{DL} at 0.22 V for the scan rate, with a corresponding ECSA of 649, 874, and 342 cm^{-2} for NMO-9, NMO-18, and NMO-27, respectively. NMO-18 exhibited the highest ECSA, consistent with its observed maximum supercapacitance. Thus, hydrothermal growth duration is critical to obtain the largest surface area and, hence, the highest supercapacitance.

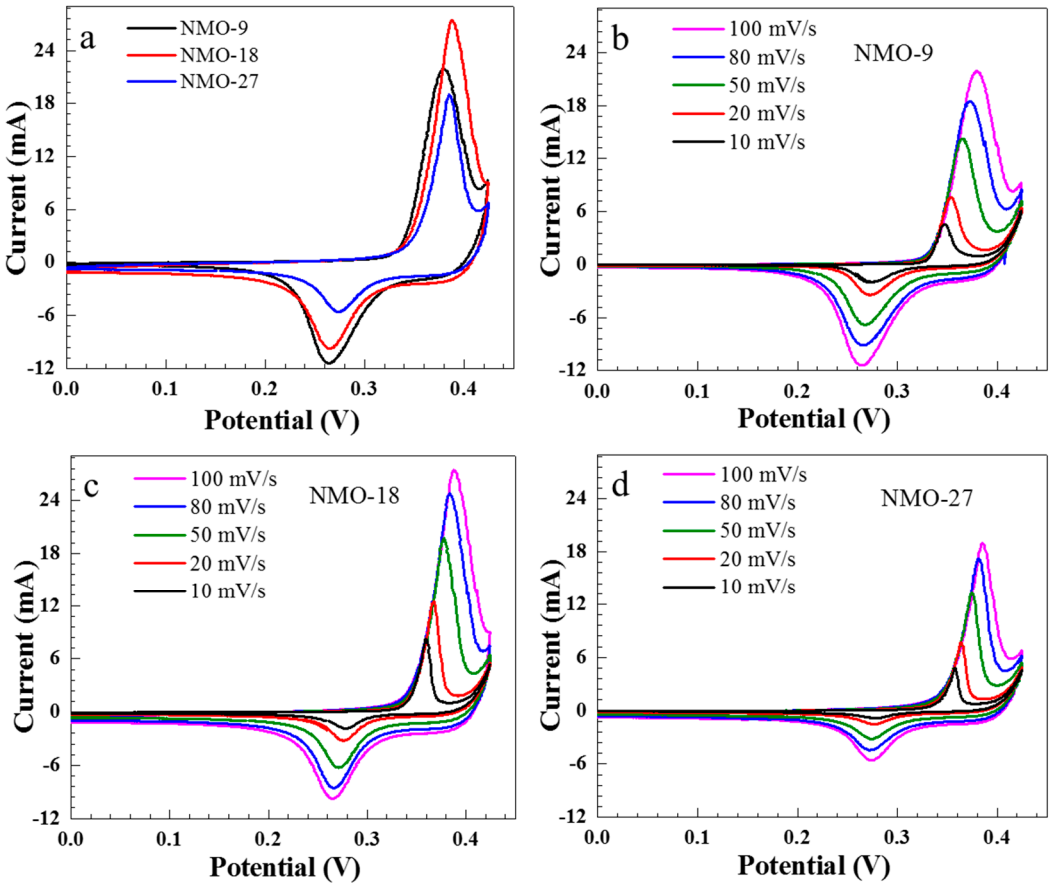

Figure 3. Cyclic voltammograms (CVs) for (**a**) NMO-9, NMO-18, and NMO-27 samples at 100 mV/s scan rate and various scan rates for (**b**) NMO-9; (**c**) NMO-18; and (**d**) NMO-27.

Figure 5a shows the galvanostatic charge-discharge profiles for the $NiMoO_4$ nanostructure electrodes at a 1 A/g current density, with NMO-18 exhibiting the longest discharge time. Figure 5b–d show NMO-9, NMO-18, and NMO-27 charge-discharge profiles, respectively, at different current densities.

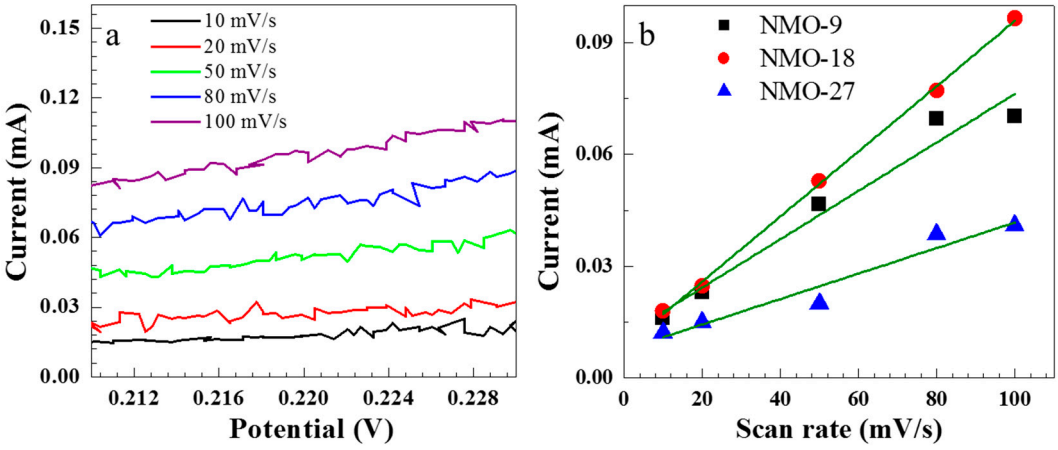

Figure 4. (**a**) Cyclic voltammograms (CV) for NMO-18 at various scan rates in the non-Faradic voltage region (0.21–0.23 V); (**b**) The measured current at 0.22 V as a function of the scan rate for NMO-9, NMO-18, and NMO-27.

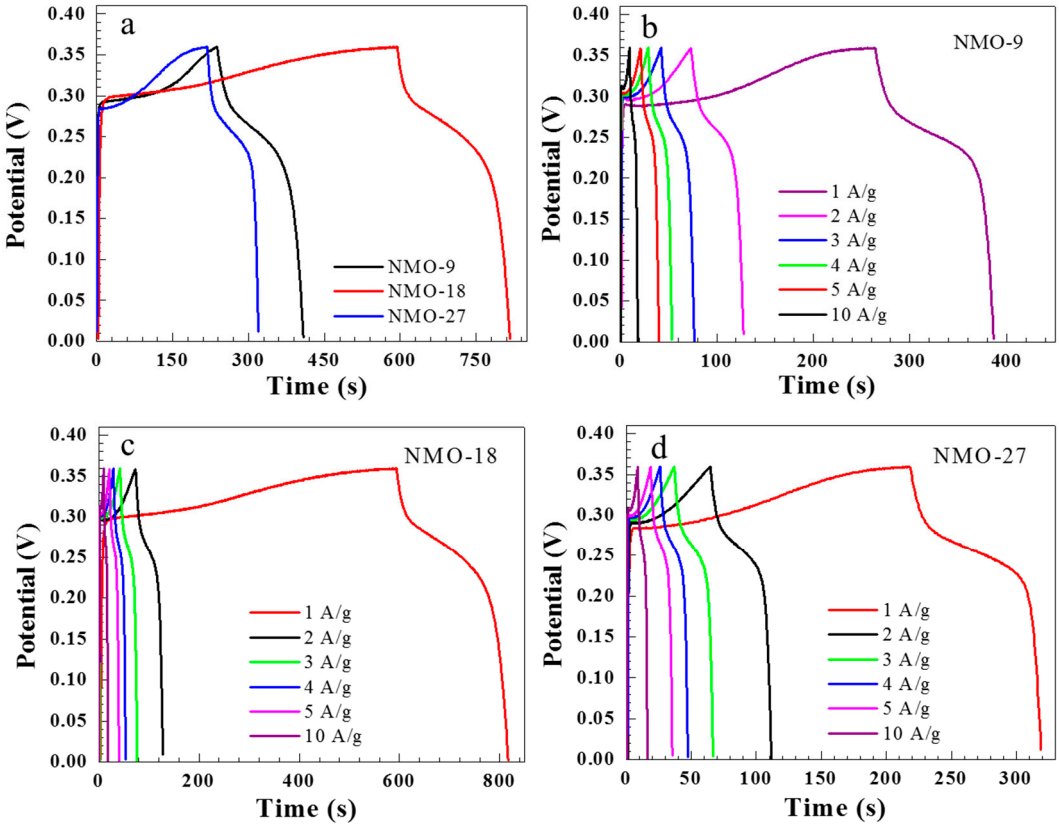

Figure 5. Galvanostatic charge-discharge profile for (**a**) NMO-9, NMO-18, and NMO-27 at 1 A/g current density; (**b**) NMO-9; (**c**) NMO-18; and (**d**) NMO-27 at various current densities.

Each charge-discharge curve shows pseudo-capacitor characteristics, consistent with the CV data. There is a sharp voltage drop as the supercapacitor changes state from charge to discharge, which can be attributed to an IR drop. Each electrode exhibits nonlinear discharge followed by a plateau, which verifies faradaic reactions occurring on the electrode surface due to the redox reaction at the material/solution interface. Figure 6a represents the specific capacitance response for current densities for all samples. The performance of the specific capacitance decreases with increasing current

density. The fall in the supercapacitance value at a high current density could be attributed to the lack of active material at the electrode/electrolyte interface during oxidation/reduction reactions and the slow diffusion of bulky OH ions [26,27].

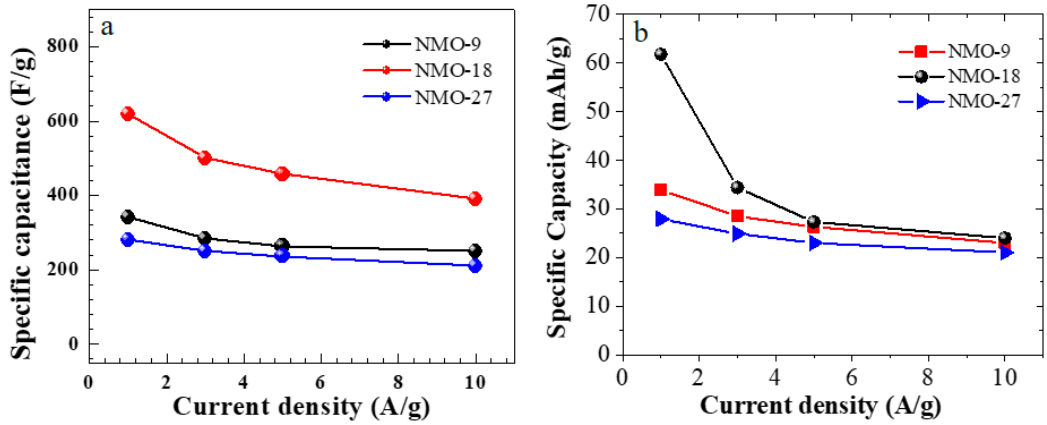

Figure 6. (**a**) Specific capacitance as a function of current density for all the samples of NMO-9, NMO-18, and NMO-27; (**b**) The response of specific capacity to current density for NMO-9, NMO-18, and NMO-27.

Specific capacitance or C_s was calculated from galvanostatic charge-discharge plots (Figure 5) from

$$C_s = \frac{I \cdot \Delta t}{m \cdot \Delta V}, \quad (3)$$

where I is the applied current density, ΔV is the potential window, and Δt is the discharge time. The calculated specific capacitances at 1 A/g are 341, 619, and 219 F/g for NMO-9, NMO-18, and NMO-27, respectively. The observed specific capacitances are directly related to the available surface area for the electrochemical reaction in the $NiMoO_4$ nanostructure electrode. The superior specific capacitance observed in NMO-18, in comparison with NMO-9 and NMO-27, can be attributed to the higher electrochemical surface area observed in NMO-18 from the ECSA estimation described above. Thus, $NiMoO_4$ nanostructures showed comparable capacitance and rate capability with previously reported materials, such as NiO [26,28], Co_3O_4 [20], and MnO_2 [29]. Table 1 shows the super capacitance values of this work along with other $NiMoO_4$ reports on various nanostructures and different substrates. The specific capacity was also calculated due to the fact that CV-plots exhibit sharp redox and oxidation peaks arising from a Faradic battery-type mechanism [30,31]. Therefore, we also present specific capacity, C (mAh/g), which can be calculated from charge-discharge plots using,

$$C = \frac{I \cdot \Delta t}{3600 \cdot m} \quad (4)$$

The specific capacity for all the samples at various current densities are shown in Figure 6b. The specific capacity for NMO-9, NMO-18, and NMO-27 are 33.9, 61.8, and 27.9 mAh/g, respectively, at a current density of 1 A/g.

Table 1. Data of previous $NiMoO_4$ nanostructure-based reports compared with our work.

S. No.	$NiMoO_4$ Electrode Type	Substrate	Substrate Type	Super Capacitance (F/g)	Reference
1.	Nanorods	Ni-Foam	Reactive	1136	[16]
2.	Nanorods	Ni-Foam	Reactive	944	[17]
3.	Nanotubes	Ni-Foam	Reactive	864	[18]
4.	Nanoneedles	Carbon	Non-reactive	412	[19]
5.	Nanograins	Stainless Steel	Non-reactive	619	This work

We also study electrochemical stability, an important characteristic for practical applications. Each $NiMoO_4$ electrode was subjected to 3000 charge-discharge cycles. Figure 7a shows the electrode stability at 10 A/g current density. NMO-18 exhibited a steep capacitance loss during the initial several hundred cycles, and then stabilized to approximately 57% retention after 3000 cycles [32]. NMO-9 and NMO-27 showed 44% and 56.5% retention after 3000 cycles of charge-discharge operations, respectively. The lower retention level in NMO-9 may be attributed to a more rapid attrition of electrode material in relation to other two samples during charge-discharge cycles. The capacitance reduction can be explained by $NiMoO_4$ material physical expansion as ionic transfer occurred and the partial dissolution of $NiMoO_4$ material during charge-discharge operations [33].

Energy density (E) and power density (P) can be expressed as

$$E = \frac{1}{2} C_S \cdot (\Delta V)^2 \quad (5)$$

and

$$P = \frac{E}{\Delta t} \quad (6)$$

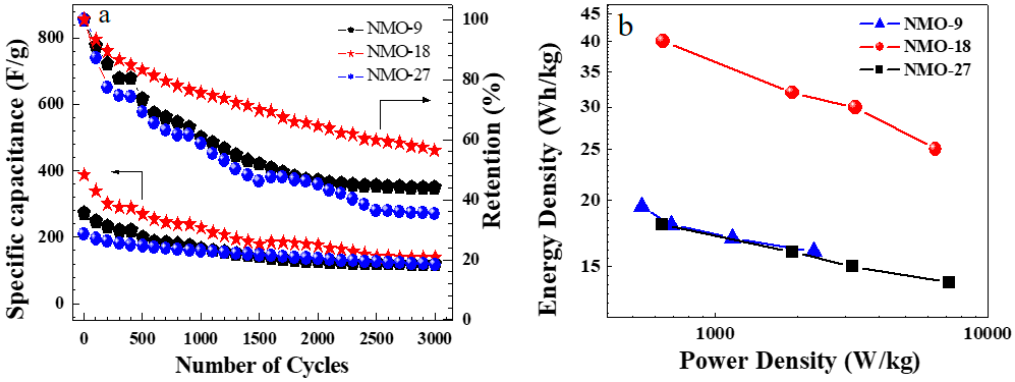

Figure 7. (**a**) Response of specific capacitance over 3000 cycles of charge-discharge operations for NMO-9, NMO-18, and NMO-27; (**b**) Ragone plots with energy density versus power density.

Figure 7b shows the Ragone plots comparing energy and power density for all the electrodes. The peak energy density was observed for NMO-18 as 40 Wh/kg, and the highest power density of 7200 W/kg was associated with NMO-27. In a largely diffusion-controlled redox reaction between NiO and OH^-, it is expected that energy density and charge-discharge rates will be inversely proportional [34–36]. It is notable that the $NiMoO_4$ nanostructures exhibited high power density and energy density, consistent with past research reports [37,38]. Table 2 shows the specific capacitance and energy density found in the current work in relation to the previously published metal oxide reports.

Table 2. Electrochemical performance of this work compared with previously reported various metal oxide supercapacitor electrode materials.

S. No.	Electrode Material	Substrate	Specific Capacitance (F/g)	Energy Density (Wh/kg)	Reference
1.	PANI/PTSa/cross linked $NiMoO_4$	Graphite	1300	60	[39]
2.	$NiMoO_4$ $CoMoO_4$ $MnMoO_4$	Carbon	412 240 120	35 15 10	[19]
3.	$CoMoO_4$	Carbon	79	21	[40]
4.	$NiMn_2O_4$/CNT	Ni	151	60.69	[41]
5.	RuO_2	-	658	-	[42]
6.	MnO_2	-	1380	-	[43]
7.	$NiMoO_4$	SS	619	40	This work

4. Conclusions

Direct $NiMoO_4$ nanostructure growth on SS substrates was achieved via a facile, single-step hydrothermal method, and the resultant electrode electrochemical characteristics were investigated with respect to growth times of 9, 18, and 27 h. The NMO-18 electrode exhibited the maximum supercapacitance value of 619, 500, 458, and 390 F/g at 1, 3, 5, and 10 A/g, respectively. All the electrodes showed good stability over 3000 charge-discharge cycles. The available active surface area for all the samples were estimated from ECSA analysis. The highest capacitance observed in NMO-18 could be attributed to the observed maximum ECSA value of the sample. Along with excellent capacitive characteristics, $NiMoO_4$ showed appreciable energy and power density values. We propose that the direct growth of nanostructured $NiMoO_4$ on SS substrate through a one-step hydrothermal method offers a promising electrode material for supercapacitor applications.

Author Contributions: V.K. did the experiment and prepared the manuscript. H.-J.K. helped with analysis and discussion. H.-C.P. helped in performing the discussion and revising the manuscript. H.-S.K. planned and supervised the project. All of the authors have discussed the results and approved the submitted version.

Funding: This work was supported by the Korea Institute of Energy Technology Evaluation and Planning (KETEP) and the Ministry of Trade, Industry & Energy (MOTIE) of the Republic of Korea (No. 20174030201520), and the Basic Science Research Program through the National Research Foundation of Korea (NRF) funded by the Ministry of Education (No. 2017R1D1A1A09000823).

Conflicts of Interest: There are no conflicts of interest to declare.

References

1. Miller, J.R.; Simon, P. Electrochemical Capacitors for Energy Management. *Science* **2008**, *321*, 651–652. [CrossRef] [PubMed]
2. Simon, P.; Gogotsi, Y. Materials for electrochemical capacitors. *Nat. Mater.* **2008**, *7*, 845–854. [CrossRef] [PubMed]
3. Liban, D.J.; Saleh, M.A.; Berkson, Z.J.; El-Kady, M.F.; Hwang, J.Y.; Mohamed, N.; Wixtrom, A.I.; Titarenko, E.; Shao, Y.; McCarthy, K.; et al. A molecular cross-linking approach for hybrid metal oxides. *Nat. Mater.* **2018**, *17*, 341–348.
4. Cheng, F.; Shen, J.; Peng, B.; Pan, Y.; Tao, Z.; Chen, J. Rapid room-temperature synthesis of nanocrystalline spinels as oxygen reduction and evolution electrocatalysts. *Nat. Chem.* **2011**, *3*, 79–84. [CrossRef] [PubMed]
5. Wu, H.B.; Pang, H.; Lou, X.W. Facile synthesis of mesoporous $Ni_{0.3}Co_{2.7}O_4$ hierarchical structures for high-performance supercapacitors. *Energy Environ. Sci.* **2013**, *6*, 3619–3626. [CrossRef]
6. Liang, Y.; Wang, H.; Zhou, J.; Li, Y.; Wang, J.; Regier, T.; Dai, H. Covalent hybrid of spinel manganese–cobalt oxide and graphene as advanced oxygen reduction electrocatalysts. *J. Am. Chem. Soc.* **2012**, *134*, 3517–3523. [CrossRef] [PubMed]
7. Zhang, J.T.; Ma, J.Z.; Zhang, L.L.; Guo, P.Z.; Jiang, J.W.; Zhao, X.S. Template synthesis of tubular ruthenium oxides for supercapacitor applications. *J. Phys. Chem. C* **2010**, *114*, 13608–13613. [CrossRef]
8. Wang, Q.H.; Jiao, L.F.; Du, H.M.; Peng, W.X.; Han, Y.; Song, D.W.; Si, Y.C.; Wang, Y.J.; Yuan, H.T. Novel flower-like CoS hierarchitectures: One-pot synthesis and electrochemical properties. *J. Mater. Chem.* **2011**, *21*, 327–329. [CrossRef]
9. Zhou, L.; He, Y.; Jia, C.; Pavlinek, V.; Saha, P.; Cheng, Q. Construction of hierarchical $CuO/Cu_2O@NiCo_2S_4$ nanowire arrays on copper foam for high performance supercapacitor electrodes. *Nanomaterials* **2017**, *7*, 273. [CrossRef] [PubMed]
10. Mai, L.Q.; Yang, F.; Zhao, Y.L.; Xu, X.; Xu, L.; Luo, Y.Z. Hierarchical $MnMoO_4/CoMoO_4$ heterostructured nanowires with enhanced supercapacitor performance. *Nat. Commun.* **2011**, *2*, 381. [CrossRef] [PubMed]
11. Liu, M.C.; Kang, L.; Kong, L.B.; Lu, C.; Ma, X.J.; Li, X.M.; Luo, Y.C. Facile synthesis of $NiMoO_4 \cdot xH_2O$ nanorods as a positive electrode material for supercapacitors. *RSC Adv.* **2013**, *3*, 6472–6478. [CrossRef]
12. Guan, B.K.; Hu, L.L.; Zhang, G.H.; Guo, D.; Fu, T.; Li, J.D.; Duan, H.G.; Li, Q.H. Facile synthesis of $ZnWO_4$ nanowall arrays on Ni foam for high performance supercapacitors. *RSC Adv.* **2014**, *4*, 4212–4217. [CrossRef]
13. Guo, D.; Zhang, P.; Zhang, H.; Yu, X.; Zhu, J.; Li, Q.; Wang, T. $NiMoO_4$ nanowires supported on Ni foam as novel advanced electrodes for supercapacitors. *J. Mater. Chem. A* **2013**, *7*, 9024–9027. [CrossRef]

14. Yu, L.; Zhang, L.; Wu, H.B.; Zhang, C.; Lou, X.W. Controlled synthesis of hierarchical $Co_xMn_{3-x}O_4$ array micro-/nanostructures with tunable morphology and composition as integrated electrodes for lithium-ion batteries. *Energy Environ. Sci.* **2013**, *6*, 2664–2671. [CrossRef]
15. Shaijumon, M.M.; Perre, E.; Daffos, B.; Taberna, P.L.; Tarascon, J.M.; Simon, P. Nanoarchitectured 3D cathodes for Li-Ion microbatteries. *Adv. Mater.* **2010**, *22*, 4978–4981. [CrossRef] [PubMed]
16. Peng, S.; Li, L.; Wu, H.B.; Madhavi, S.; Lou, X.W. Controlled growth of $NiMoO_4$ nanosheet and nanorod arrays on various conductive substrates as advanced electrodes for asymmetric supercapacitors. *Adv. Energy Mater.* **2015**, *5*, 1401172. [CrossRef]
17. Cai, D.; Wang, D.; Liu, B.; Wang, Y.; Liu, Y.; Wang, L.; Li, H.; Huang, H.; Li, Q.; Wang, T. Comparison of the electrochemical performance of $NiMoO_4$ nanorods and hierarchical nanospheres for supercapacitor applications. *ACS Appl. Mater. Interface* **2013**, *5*, 12905–12910. [CrossRef] [PubMed]
18. Yin, Z.; Zhang, S.; Chen, Y.; Gao, P.; Zhu, C.; Yang, P.; Qi, L. Hierarchical nanosheet-based $NiMoO_4$ nanotubes: Synthesis and high supercapacitor performance. *J. Mater. Chem. A* **2015**, *3*, 739–745. [CrossRef]
19. Teeraphat, W.; Manickam, M.S.; Sudip, C.; Dan, L.; Shafiullah, G.M.; Robert, D.A.; Rajeev, A. Effect of transition metal cations on stability enhancement for molybdate-based hybrid supercapacitor. *ACS Appl. Mater. Interfaces* **2017**, *9*, 17977–17991.
20. Meher, S.K.; Rao, G.R. Ultralayered Co_3O_4 for high-performance supercapacitor applications. *J. Phys. Chem. C* **2011**, *115*, 15646–15654. [CrossRef]
21. Chen, J.S.; Ng, M.F.; Wu, H.B.; Zhang, L.; Lou, X.W. Synthesis of phase-pure SnO_2 nanosheets with different organized structures and their lithium storage properties. *CrystEngComm* **2012**, *14*, 5133–5136. [CrossRef]
22. Zhang, G.Q.; Lou, X.W. General solution growth of mesoporous $NiCo_2O_4$ nanosheets on various conductive substrates as high-performance electrodes for supercapacitors. *Adv. Mater.* **2013**, *25*, 976–979. [CrossRef] [PubMed]
23. Qu, B.H.; Chen, Y.J.; Zhang, M.; Hu, L.L.; Lei, D.N.; Lu, B.G.; Li, Q.H.; Wang, Y.G.; Chen, L.B.; Wang, T.H. β-Cobalt sulfide nanoparticles decorated graphene composite electrodes for high capacity and power supercapacitors. *Nanoscale* **2012**, *4*, 7810–7816. [CrossRef] [PubMed]
24. Yan, J.; Fan, Z.J.; Sun, W.; Ning, G.Q.; Wei, T.; Zhang, Q.; Zhang, R.F.; Zhi, L.J.; Wei, F. Advanced asymmetric supercapacitors based on $Ni(OH)_2$/graphene and porous graphene electrodes with high energy density. *Adv. Funct. Mater.* **2012**, *22*, 2632–2641. [CrossRef]
25. Charles, C.L.M.; Jung, S.; Jonas, C.P.; Thomas, F.J. Benchmarking heterogeneous electrocatalysts for the oxygen evolution reaction. *J. Am. Chem. Soc.* **2013**, *135*, 16977–16987.
26. Qian, H.; Jinlong, L.; Tongxiang, L.; Chen, W. In situ synthesis of mesoporous $NiMoO_4$ on ball milled graphene for high performance supercapacitors. *J. Electrochem. Soc.* **2017**, *164*, E173–E179. [CrossRef]
27. Hatzell, K.B.; Beidaghi, M.; Campos, J.W.; Dennison, C.R.; Kumbur, E.C.; Gogotsi, Y. A high performance pseudocapacitive suspension electrode for the electrochemical flow capacitor. *Electrochim. Acta* **2013**, *111*, 888–897. [CrossRef]
28. Han, D.D.; Xu, P.C.; Jing, X.Y.; Wang, J.; Yang, P.P.; Shen, Q.H.; Liu, J.Y.; Song, D.L.; Gao, Z.; Zhang, M.L. Trisodium citrate assisted synthesis of hierarchical NiO nanospheres with improved supercapacitor performance. *J. Power Sources* **2013**, *235*, 45–53. [CrossRef]
29. Yu, G.H.; Hu, L.B.; Vosgueritchian, M.; Wang, H.L.; Xie, X.; McDonough, J.R.; Cui, X.; Cui, Y.; Bao, Z.N. Solution-processed graphene/MnO_2 nanostructured textiles for high-performance electrochemical capacitors. *Nano Lett.* **2011**, *11*, 2905–2911. [CrossRef] [PubMed]
30. Brousse, T.; B'elanger, D.; Longd, J.W. To be or not to be pseudocapacitive? *J. Electrochem. Soc.* **2015**, *162*, A5185–A5189. [CrossRef]
31. Owusu, K.A.; Qu, L.; Li, J.; Wang, Z.; Zhao, K.; Yang, C.; Hercule, K.M.; Lin, C.; Shi, C.; Wei, Q.; et al. Low-crystalline iron oxide hydroxide nanoparticle anode for high-performance supercapacitors. *Nat. Commun.* **2017**, *8*, 14264. [CrossRef] [PubMed]
32. Liu, M.C.; Kong, L.B.; Lu, C.; Ma, X.J.; Li, X.M.; Luo, Y.C.; Kang, L. Design and synthesis of $CoMoO_4$–$NiMoO_4 \cdot xH_2O$ bundles with improved electrochemical properties for supercapacitors. *J. Mater. Chem. A* **2013**, *1*, 1380–1387. [CrossRef]
33. He, Y.M.; Chen, W.J.; Li, X.D.; Zhang, Z.X.; Fu, J.C.; Zhao, C.H.; Xie, E.Q. Freestanding three-dimensional graphene/MnO_2 composite networks as ultralight and flexible supercapacitor electrodes. *ACS Nano* **2013**, *7*, 174–182. [CrossRef] [PubMed]

34. Prasad, K.R.; Miura, N. Electrochemically deposited nanowhiskers of nickel oxide as a high-power pseudocapacitive electrode. *Appl. Phys. Lett.* **2004**, *85*, 4199–4201. [CrossRef]
35. Brezesinski, T.; Wang, J.; Polleux, J.; Dunn, B.; Tolbert, S.H. Templated nanocrystal-based porous TiO_2 films for next-generation electrochemical capacitors. *J. Am. Chem. Soc.* **2009**, *131*, 1802–1809. [CrossRef] [PubMed]
36. Zheng, J.P.; Jow, T.R. High energy and high power density electrochemical capacitors. *J. Power Sources.* **1996**, *62*, 155–159. [CrossRef]
37. Wang, H.L.; Gao, Q.M.; Jiang, L. Facile approach to prepare nickel cobaltite nanowire materials for supercapacitors. *Small* **2011**, *7*, 2454–2459. [CrossRef] [PubMed]
38. Jiang, H.; Li, C.Z.; Sun, T.; Ma, J. High-performance supercapacitor material based on $Ni(OH)_2$ nanowire-MnO_2 nanoflakes core–shell nanostructures. *Chem. Commun.* **2012**, *48*, 2606–2608. [CrossRef] [PubMed]
39. Ramkumar, R.; Sundaram, M.M. Electrochemical synthesis of polyaniline crosslinked $NiMoO_4$ nanofibre dendrites for energy storage devices. *New J. Chem.* **2016**, *40*, 7456–7464. [CrossRef]
40. Barmi, M.J.; Minakshi, M. Tuning the redox properties of the nanostructured $CoMoO_4$ electrode: effects of surfactant content and synthesis temperature. *ChemPlusChem* **2016**, *81*, 964–977. [CrossRef]
41. Nan, H.; Ma, W.; Gu, Z.; Geng, B.; Zhang, X. Hierarchical $NiMn_2O_4$@CNT nanocomposites for high-performance asymmetric supercapacitors. *RSC Adv.* **2015**, *5*, 24607–24614. [CrossRef]
42. Sugimoto, W.; Iwata, H.; Yasunaga, Y.; Murakami, Y.; Takasu, Y. Preparation of ruthenic acid nanosheets and utilization of its interlayer surface for electrochemical energy storage. *Angew. Chem. Int. Ed.* **2003**, *42*, 4092–4096. [CrossRef] [PubMed]
43. Toupin, M.; Brousse, T.; Be'langer, D. Charge storage mechanism of MnO_2 electrode used in aqueous electrochemical capacitor. *Chem. Mater.* **2004**, *16*, 3184–3190. [CrossRef]